Correlation-driven nontrivial phases in single-bilayer kagome intermetallics

Aabhaas Vineet Mallik [1,*] Adhip Agarwala [2,†] and Tanusri Saha-Dasgupta [3,‡]
[1]*Department of Physics, Bar-Ilan University, Ramat Gan 5290002, Israel*
[2]*Indian Institute of Technology Kanpur, Kalyanpur, Kanpur 208016, India*
[3]*Department of Condensed Matter Physics and Materials Science, S. N. Bose National Centre for Basic Sciences, Kolkata 700098, India*

(Received 16 July 2023; revised 26 September 2023; accepted 10 October 2023; published 13 November 2023)

Bilayer kagome compounds provide an exciting playground where the interplay of topology and strong correlations can give rise to exotic phases of matter. Motivated by recent first-principles calculation on such systems [Phys. Rev. Lett. **125**, 026401 (2020)], reporting stabilization of a Chern metal with a topological nearly flat band close to the Fermi level, we build minimal models to study the effect of strong electron-electron interactions on such a Chern metal. Using appropriate numerical and analytical techniques, we show that the topologically nontrivial bands present in this system at the Fermi energy can realize fractional Chern insulator states. We further show that if the time-reversal symmetry is restored due to the destruction of magnetism by low dimensionality and fluctuation, the system can realize a superconducting phase in the presence of strong local repulsive interactions. Furthermore, we identify an interesting phase transition from the superconducting phase to a correlated metal by tuning nearest-neighbor repulsion. Our study uncovers a rich set of nontrivial phases realizable in this system and contextualizes the physically meaningful regimes where such phases can be further explored.

DOI: 10.1103/PhysRevB.108.205125

I. INTRODUCTION

The kagome lattice—built out of corner sharing triangles—presents a rather interesting situation where both the itinerancy of the electrons as well as the effect of electron-electron interactions, can be frustrated. The frustration of the itinerant electrons is manifested through the characteristic flat/nearly flat bands in the various short-range tight-binding models on the kagome lattice. When the Fermi energy lies in one of these bands of narrow bandwidth then the electron-electron interactions are expected to play a crucial role in determining the ground state properties of the system. Together with this effect, the presence of spin-orbit coupling in the nearly flat noninteracting band at the Fermi energy may lead to a nontrivial band topology [1–6]. This interplay of electron-electron interactions and band topology poses outstanding challenges and has been of much interest, for example, in the context of fractionally filled Landau levels in the quantum Hall systems [7–9] and Moire graphene [10,11] more recently. Interestingly, a plethora of recently discovered metallic systems based on the kagome motif [12–32] provide a wide material basis to realize and explore this physics further.

A particularly interesting family of kagome based metallic systems occurs in the binary intermetallics M_3Sn_2, where M = Mn, Fe, Ni, Cu, and Co represents a transition metal [12–23,33–35]. These materials form a three dimensional layered structure with the basic motif being a bilayer kagome of the M atoms, as shown in Fig. 1. The sought-after flat bands have been observed in iron compounds [21], in cobalt systems [36,37], and most recently in manganese based intermetallics [38,39]. The interplay of strong correlations and topological properties is manifested in a wide range of observed exotic phenomena, such as the coexistence of magnetism and anomalous Hall effect seen recently in manganese systems (along with rare earths) [40], an exotic charge density wave order and superconductivity seen in related antimony compounds [25–27,41–43]. A variety of other observations including skyrmions and topological Hall effect [44], hole pockets at the Fermi surface [45], and spin waves [46] have further made the field extremely intriguing.

An especially intriguing system in this family are the FeSn compounds where the stacking arrangement can alter the nature of both the magnetic properties of the ground state as well as that of the itinerant electrons. For instance, when the two kagome Fe_3Sn layers in a bilayer motif are aligned such that the Fe atoms in the two layers are right on top of each other, the system is antiferromagnetic with strong spin fluctuations and localized electrons [47–49]. On the other hand when the two Fe_3Sn layers are aligned such that Fe atoms in the two layers form a star of David (see Fig. 1), the system is ferromagnetic with a flat band near the Fermi energy which is topological in nature making it susceptible towards a host of exotic phenomena [14,50,51]. Given the susceptibility of this latter system to a host of exotic phases it forms the focus of our study in this paper. More specifically, we focus on the single bilayer limit. As shown in one of our previous works [51] cleavability of these compounds, allows possible synthesis of single bilayer and its tunability, for example, by using different substrates [33,50]. The situation is

*aabhaas.iiser@gmail.com
†adhip@iitk.ac.in
‡t.sahadasgupta@gmail.com

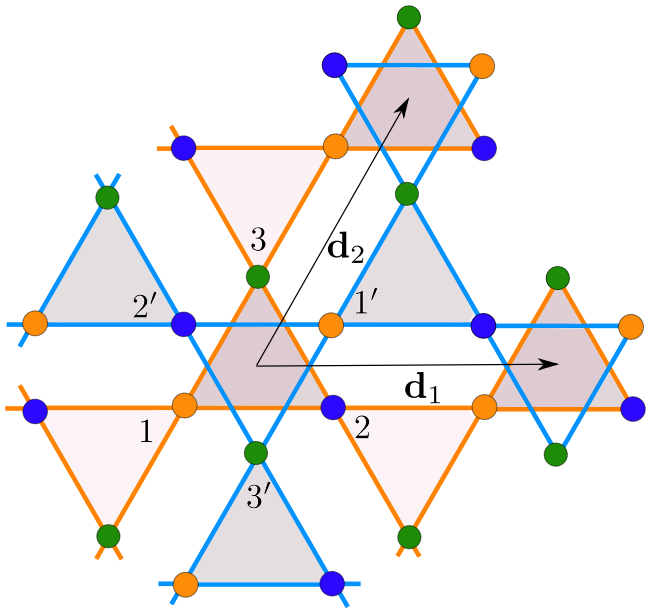

FIG. 1. *Bilayer kagome lattice*. A kagome bilayer lattice has a tripartite structure with a unit cell containing six identical atoms labeled (1-3) (bottom layer) and (1′-3′) (top layer) and shown by different colors. Inter- and intra-unit-cell nearest-neighbor hoppings can have different hopping strengths due to breathing anisotropy. The lattice vectors are given by $\mathbf{d}_1 = \{1, 0\}$, $\mathbf{d}_2 = \{\frac{1}{2}, \frac{\sqrt{3}}{2}\}$. The reciprocal lattice vectors are given by $\mathbf{b}_1 = \{\frac{\sqrt{3}}{2}, -\frac{1}{2}\}\frac{4\pi}{\sqrt{3}}$, $\mathbf{b}_2 = \{0, 1\}\frac{4\pi}{\sqrt{3}}$.

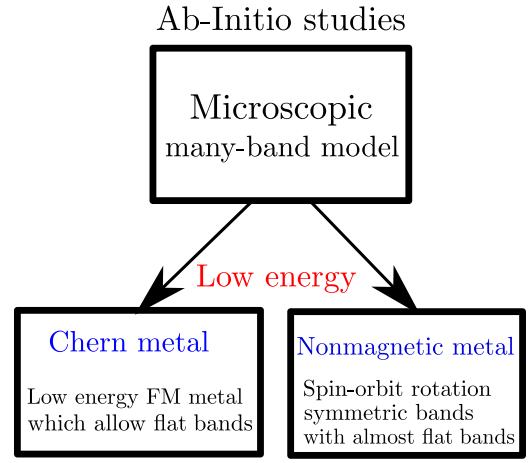

FIG. 2. *Effective low-energy physics. Ab initio* studies lead to two broad category of microscopically interesting systems (i) Chern metals—which spontaneously breaks time-reversal symmetry and have a partially filled flat band with a nonzero Chern number, and (ii) nonmagnetic metals—a metallic phase which retains the complete spin-orbit rotation symmetry.

further promising as such epitaxial films have recently been synthesized [52].

Although, the experiments and first-principles calculation for the bulk Fe_3Sn_2 [14,51] reveal a complicated band structure close to the Fermi energy, interestingly, in the single-bilayer limit, a simplified low-energy band structure separated from the high-energy bands emerges. This allows for the possibility of analyzing the low-energy physics of the single bilayer systems using effective tight-binding models with short-range electron-electron interactions [51]. In the bilayer limit, the first-principles calculation [51] found the Fe based system to be a Chern metal, while the Ni/Co based system to be nonmagnetic. With these first-principles inputs, it will be a worthwhile exercise to understand the possible interaction-driven instabilities towards nontrivial phases in the nearly flat bands of the spin-polarized Chern metal as well as the nonmagnetic metal.

In this paper, we take up the above task within the framework of a minimal symmetry allowed hopping Hamiltonian, characterized by interlayer hybridization, intralayer breathing distortion due to differently sized up and down triangles, and interlayer potential difference. The microscopic many-body model built up on this, hosting flat-bands is studied for both (a) a low-energy Chern metal and (b) a low-energy nonmagnetic metal, as shown in Fig. 2. Our analysis establishes that possible tuning of these parameters by substrate effect, strain as well as gating, can give rise to a plethora of correlation-driven exotic phases. For the Chern metal, when the two kagome layers are weakly hybridized, the repulsive interactions in the ferromagnetic flat-band can stabilize a 1/3 fractional Chern insulator (FCI) state, while possibly stabilizing a 1/5 FCI state in the limit of strong interlayer hybridization. On the other hand, in the case of nonmagnetic metal, we discover a pairing instability in the presence of strong onsite repulsion within a t-J-V model calculation. The transition temperature of the corresponding superconducting phase can be as high as about 30 K. Upon varying the strength of the repulsive interactions, a transition to a correlated metallic phase is discussed which can possibly host a chiral spin liquid akin to that found on the triangular lattice in Ref. [53].

While our work is motivated by the bilayer physics of Fe_3Sn_2, the analysis presented here is general in nature and should be applicable to a range of bilayer kagome thin films.

II. LOW-ENERGY HAMILTONIANS FOR BILAYER KAGOME METALS

A minimal symmetry allowed hopping Hamiltonian, consisting of one Kramers doublet per site (Fig. 1), is given by

$$H_{tb} = \sum_{ij,\sigma} t_{ij}^{\sigma} c_{i\sigma}^{\dagger} c_{j\sigma} - \mu \sum_{i} n_i, \tag{1}$$

where i and j refer to the sites on the bilayer kagome lattice, $c_{i\sigma}$ ($c_{i\sigma}^{\dagger}$) are the electron annihilation (creation) operators at site i with spin $\sigma = \uparrow, \downarrow$ and $n_i = \sum_{\sigma} c_{i\sigma}^{\dagger} c_{i\sigma}$ is the onsite electron number operator. t_{ij}^{σ} denote various hopping amplitudes (see Fig. 3), including an effective spin-orbit coupling term, and μ is the chemical potential.

In this paper, we shall use this single orbital hopping Hamiltonian H_{tb} to study the competition between various relevant phases. Such an approach has proved to be fruitful in understanding a host of flat-band systems, e.g., in various Moire structures [54]. It is worth noting that the above minimal model has several parameters which in principle can be tuned in the experiments on the bilayer kagome materials. Below we list the important model parameters and mention the range of their expected tunability from studies on closely related material systems.

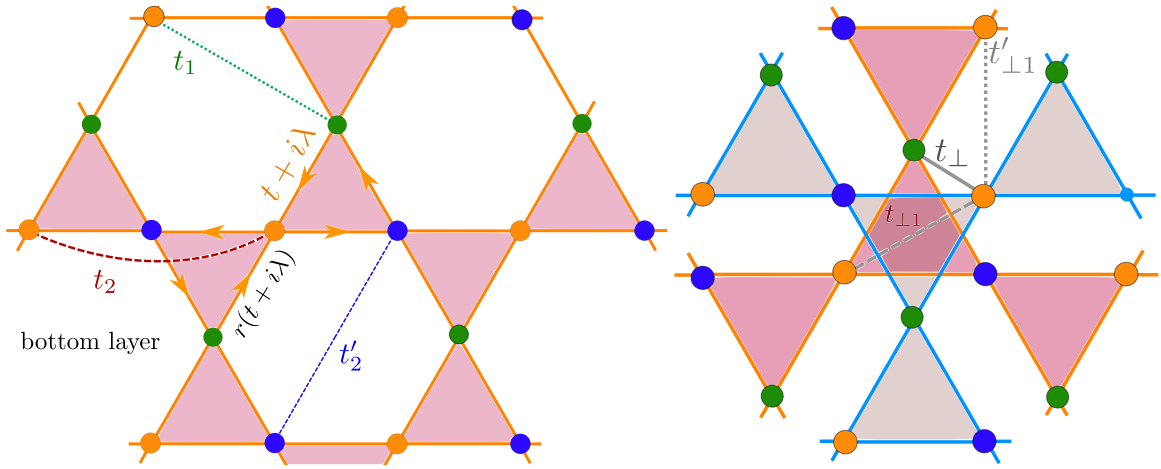

FIG. 3. *Hopping processes.* The left and right panels depict the intralayer and interlayer hoppings for an up-spin electron in a bilayer kagome system. The hoppings for the down-spin electrons can be obtained by switching the sign of λ. Note that all the kagome sites are equivalent. Different colors have been used to highlight the tripartite structure.

(1) The nearest-neighbor hopping amplitude t(∼0.1 eV for Fe_3Sn_2 [51], ∼0.2 eV for CoSn [37]) can possibly be tuned using strain [55].

(2) The chemical potential μ which controls the filling and can be changed, for example, using gating techniques and chemical doping [24].

(3) A relative potential difference between the two layers D breaks the inversion symmetry of the system and can be used to model the choice of the substrate. Such effects may be important in epitaxially grown films [56].

(4) The symmetry consistent breathing anisotropy between the up and the down triangles of each kagome layer, shown as two differently shaded triangles in Fig. 1, which gives rise to two different sized triangles. This effect is incorporated by scaling the intralayer inter-unit-cell hopping amplitude by a factor r compared to the intra-unit-cell hopping in the same layer. In experiments the ratio of the intra-unit-cell and inter-unit-cell bond lengths can be ∼0.7 in some kagome compounds [57] and can also be tuned by applying anisotropic pressure [58] or by the use of appropriate substrates [59].

(5) The hopping amplitudes $t_\perp$, $t_{\perp 1}$, and $t'_{\perp 1}$ model the various short-ranged interlayer hybridization strengths. While, $t_\perp$ is expected to be around (∼0.3t) in bilayer FeSn compounds [14,60], it can be tuned by the application of pressure [58] or by applying an uniaxial strain.

(6) We model the effect of atomic spin-orbit coupling, expected to be present in these intermetallics [51], by including a nearest-neighbor intralayer hopping process with an imaginary amplitude

$$i\lambda(c^\dagger_{i\uparrow}c_{j\uparrow} - c^\dagger_{i\downarrow}c_{j\downarrow}), \tag{2}$$

where $j \to i$ has an anticlockwise orientation over any triangular motif. In a related system such a λ is known to be ∼30–40 meV [14,60,61] and about ∼0.1 eV in CoSn [37].

Before moving on to discuss the effect of electron-electron interactions, we would like to discuss the salient features of such a symmetry consistent tight-binding Hamiltonian. A representative band structure obtained within our one-orbital-per-site model is shown in Fig. 4. Most remarkable is the occurrence of an isolated nearly *flat band* at the Fermi energy, which captures the large density of states also seen from the first-principles results for Fe_3Sn_2 [51]. In the absence of spin-orbit coupling λ [Eq. (2)], the nearly flat band touches the dispersing band at the K point of the Brillouin zone (BZ). This degeneracy, however, is generically lifted for any finite λ owing to the difference in the symmetries of the model Hamiltonian in the presence and in the absence of the λ term (details in Appendix A). In other words, for a nonzero λ, our minimal tight-binding model is generically expected to host an isolated nearly flat band. In the next section, we discuss the role of interactions on this nearly flat tight-binding band.

A. Interactions

Short-ranged microscopic interactions on the low-energy electrons are given by a generalized Hubbard model of the

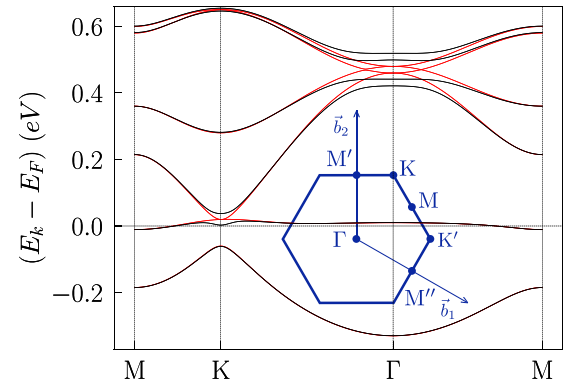

FIG. 4. *Representative band structure.* A representative band structure of the minimal symmetry allowed hopping Hamiltonian, with the choice of $t = 0.12$ eV, $r = 1.25$, $t_\perp = 0.06$ eV, $t_1 = -0.03$ eV, $t_{\perp 1} = 0.05$ eV, $\mu = -0.26$ eV, and $\lambda = 0.01$ eV (see text for further details). The corresponding band structure switching off the spin-orbit coupling ($\lambda = 0$) is shown for comparison (in red). The inset shows the high symmetry points and the reciprocal lattice vectors in a hexagonal Brillouin zone.

form

$$H_{\text{int}} = U \sum_i n_{i\uparrow} n_{i\downarrow} + \sum_{ij} V_{ij} n_i n_j, \tag{3}$$

where $n_{i\uparrow(\downarrow)}$ is the electron number operator at site i with spin up (down), while $n_i = n_{i\uparrow} + n_{i\downarrow}$ is the total electron number operator at the site i. U is the onsite repulsive interaction strength and V_{ij} represent the off-site nearest neighbor (both intra- and interlayer) density-density interactions between the electrons at sites i and j.

1. The ferromagnetic Chern metal

First-principles calculations suggest that the bilayer Fe_3Sn_2 should stabilize a ferromagnetic ground state [51]. Such a ferromagnetic state can indeed be favored by the onsite term in Eq. (3) as is demonstrated within the following mean-field analysis [62]:

$$U n_{i\uparrow} n_{i\downarrow} = \frac{U}{2}\left(n_{i\uparrow} + n_{i\downarrow} - \frac{4}{3}(\boldsymbol{S}_i \cdot \boldsymbol{S}_i)\right) \to -\frac{4U}{3}\mathbf{m} \cdot \mathbf{S}_i + \cdots, \tag{4}$$

where $S_i^{(\tau)} = \frac{1}{2}\sum_{ss'} c_{is}^\dagger \sigma_{ss'}^{(\tau)} c_{is'}$ are the electron spin operators with $\sigma^{(\tau)}$ being the Pauli matrices and $\mathbf{m} = \langle \mathbf{S}_i \rangle$ is the uniform mean-field magnetization which we take to be along the z axis, i.e., $m_z = \frac{1}{N}\sum_i \langle S_i^z \rangle \neq 0$, $m_x = m_y = 0$. While ignoring the effect of the subdominant nearest-neighbor interactions V_{ij}, self-consistent mean-field calculations for tight-binding parameters presented in Fig. 4 indicate that $U \gtrsim t$ is sufficient to completely spin polarize the bands close to the Fermi energy (see Appendix B).

A few representative band structures deep in the ferromagnetic phase, where the bands close to the Fermi energy are fully spin polarized, are presented in Fig. 5. Figure 5(a) shows a representative example in the weak interlayer hybridization limit (see caption for the parameters), while Fig. 5(b) shows an example in the strong interlayer hybridization limit (see caption for the parameters). Remarkably, in both these limits, the resultant low-energy bands are endowed with nontrivial Chern numbers (C) as shown in the figure. These two classes of band structures are robust over a finite window of $\lambda \neq 0$ as well as other parameters. The two $C = 1$ bands in the weak coupling limit, can almost exclusively be associated with one of the kagome layers [63]; one band from each of the kagome layers. Interestingly, however, on increasing the interlayer hybridization, the two $C = 1$ bands undergo a Dirac gap closing at the K' point [see Fig. 5(c)]. With further increase in the interlayer hybridization the gap reopens giving rise to a topologically trivial band and a $C = 2$ band at the Fermi level.

In what follows, we shall devote our attention to the above weak and strongly hybridized low-energy Chern bands of reduced bandwidth to explore the effect of interactions on the Chern metal. We note, however, that strong quantum fluctuations arising specially from reduced dimensionality of the bilayer may destabilize the ferromagnetic metal in favor of a nonmagnetic one. This provides a completely different starting point for exploring the effect of electron-electron interactions on unpolarized nontopological flat bands. In the next couple of sections, we shall consider these two different classes separately and investigate the interesting phases that can possibly be realized.

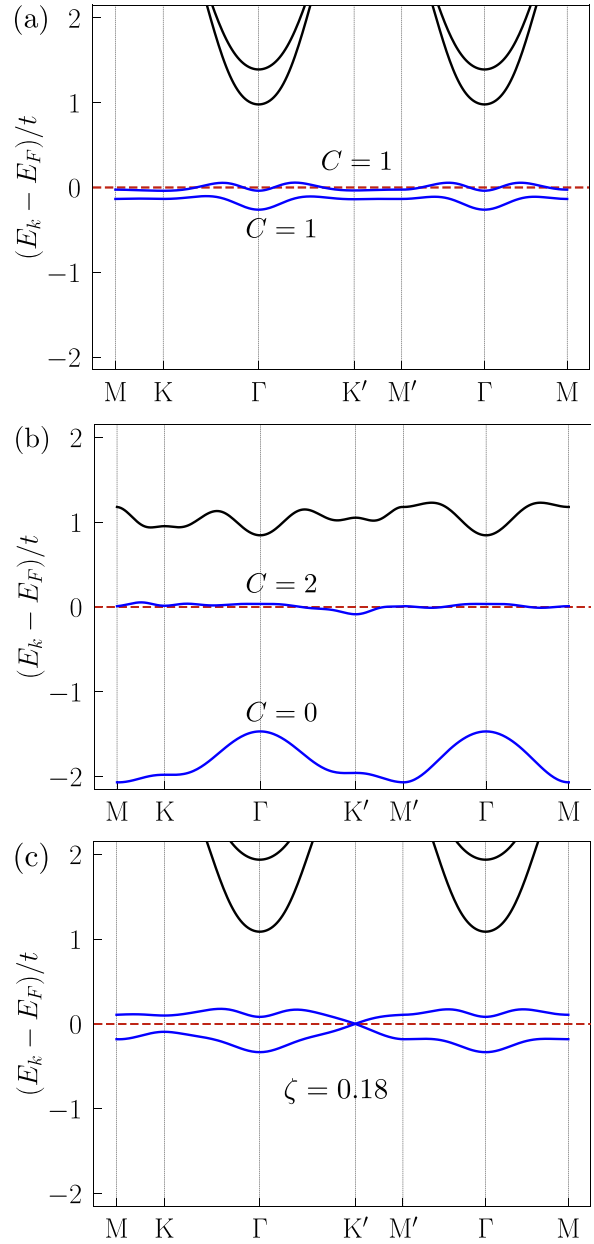

FIG. 5. *Weak and strong hybridization.* (a) The low-energy tight-binding bands in the weak interlayer coupling limit ($r = 1.0$, $t_\perp/t = 0.1$, $t_1/t = -0.2$, $t_{\perp 1}/t = -0.1$, $t'_{\perp 1}/t = 0.0$, $\lambda/t = 1.0$ and $D/t = 0.1$), denoted by Hamiltonian, H_I. (b) The low-energy tight-binding bands in the strong interlayer coupling limit ($r = 0.9$, $t_\perp/t = 0.7$, $t_1/t = -0.3$, $t_{\perp 1}/t = 0.25$, $t'_{\perp 1}/t = -0.5$, $\lambda/t = 0.3$, and $D/t = 0.1$), denoted by Hamiltonian, H_{II}. (c) The low-energy bands for $H_\zeta \equiv H_I + \zeta(H_{II} - H_I)$ ($\zeta \sim 0.18$), exhibiting a Dirac crossing at the K' point.

III. FRACTIONAL CHERN INSULATING PHASES

For the electrons in the spin-polarized nearly flat Chern band of the ferromagnetic metal, short-range interactions can lead to a host of novel phases some of which we explore

in this section. The electronic Chern metal has an instability for attractive nearest-neighbor interactions which stabilizes a topological superconductor, as was previously discussed in [51]. We now discuss the instabilities of the Chern metal to repulsive interactions such as the nearest-neighbor density-density repulsion in Eq. (3). A simple analysis suggests that such interactions cannot stabilize a superconducting phase within the mean-field approximation (see Appendix C for a discussion). In this section, we focus our investigation towards the possibility of realizing the fractional Chern insulator (FCI) states driven by these nearest-neighbor density-density interactions in the kagome bilayer.

Robust FCI states often arise as an interaction driven instability of a fractionally filled Chern band at a particular filling of $1/(2m+1)$ with m being an integer [64]. Moreover, for a topological band with Chern number C one expects the FCI states at an electronic filling of $1/(2C+1)$ to be the most robust [65]. This expectation is borne out by several numerical studies on different lattice systems [66–68], and as we show below, it holds good for our bilayer kagome as well.

To examine this instability we perform exact diagonalization (ED) studies while incorporating *both* intralayer nearest-neighbor interactions $\equiv V_{\parallel}$ and interlayer nearest-neighbor interactions $\equiv V_{\perp}$. Proceeding conventionally [64], we drop the dispersion of the band at the Fermi energy and project the interactions to just this flat band while ignoring the Hartree terms from the projected interactions. These approximations allows us to distill signatures of the FCI states within our ED studies. Our ED studies are performed in the momentum space where the Hamiltonian is block diagonal in total Bloch momentum [64]. We are, however, limited to a momentum grid of $\sim$35 points for which the low-energy eigenspectrum can be obtained efficiently.

The considerations described above lead to the following effective Hamiltonian:

$$H_{\mathrm{FCI}} = \mathcal{P} \sum_{\substack{\mathbf{k}_1,\mathbf{k}_2,\mathbf{k}_3,\mathbf{k}_4 \\ \alpha_1,\alpha_2,\alpha_3,\alpha_4}} V^{\alpha_1,\alpha_2,\alpha_3,\alpha_4}_{\mathbf{k}_1,\mathbf{k}_2,\mathbf{k}_3,\mathbf{k}_4} c^{\dagger}_{\mathbf{k}_1,\alpha_1} c^{\dagger}_{\mathbf{k}_2,\alpha_2} c_{\mathbf{k}_3,\alpha_3} c_{\mathbf{k}_4,\alpha_4} \mathcal{P}, \quad (5)$$

where the sums over $\mathbf{k}$'s run over the Bloch momenta in the first Brillouin zone while the sums over α's run over the six bands of our spin-polarized bilayer kagome system and $\mathcal{P}$ implements the projection to the band at the Fermi energy. In this context, it is convenient [64] to map a Bloch momentum $\mathbf{k} = k_x \mathbf{b}_1 + k_y \mathbf{b}_2$, where $\mathbf{b}_{1(2)}$ is a reciprocal lattice vector (see inset of Fig. 4) and $k_{x(y)} = 2\pi K_{x(y)}/N_{x(y)}$ with $N_{x(y)}$ being the number of unit cells along the lattice vector $\mathbf{d}_{1(2)}$ (see Fig. 1) and $K_{x(y)} \in \{0, 1, \ldots, N_{x(y)} - 1\}$, uniquely to the integer $K_x + N_x K_y$. For the results presented in this section we shall use this map to resolve the eigen spectrum of Eq. (5) in the different total Bloch momentum sectors.

Moreover, since we completely ignore the weak dispersion of the tight-binding band, $V_{\perp}$ and $V_{||}$ are the only relevant energy scales in the problem. To streamline the discussion further we set $V_{\perp} = V_{||}$ and report the energies of the many-body states obtained from our exact diagonalization studies in the units of $V_{\perp}$ $(= V_{||})$. Small deviations from $V_{\perp}/V_{||} = 1$ does not effect our main findings. Furthermore, given the tunability of the tight-binding parameters (discussed in Sec. II) real materials can possibly realize much flatter bands with nontrivial Chern numbers which are separated from the other bands in the system by a gap which is greater than $V_{\perp}$. We must point out, though, that FCI states can exist even if the flat Chern band at the Fermi energy is not sufficiently isolated from the other bands in the system (see, for example, Ref. [69]). Thus we believe that the FCI states that we uncover are representatives of similar and possibly more robust FCI states realizable in distinct tight-binding parameter regimes of the bilayer kagome system.

1. **1/3** *fractional Chern insulator*

In the weak interlayer hybridization limit of Fig. 5(a), we project the interactions on to the second lowest (energy) Chern band with $C = 1$. At 1/3rd filling of this band our exact diagonalization (ED) of H_{FCI} [Eq. (5)] reveals compelling characteristic features of the 1/3 FCI state.

With periodic boundary conditions we find a threefold quasidegenerate ground state manifold and a finite gap to excitations [see Fig. 6(a)]. Moreover, the total momentum of each state in the ground state manifold is exactly as predicted by the generalized Pauli principle (see Appendix D). When a flux Φ is introduced via twisted boundary conditions the threefold quasidegenerate ground state manifold remains separated from the excited states while exhibiting a twist angle periodicity of 6π, confirming their 1/3 FCI character [see Fig. 6(b)] [64]. We also find that for the states in the ground state manifold $\langle n_k \rangle$, occupancy of the single particle Bloch state with crystal momentum k in the band at the Fermi energy, equals $\sim$1/3 [see Fig. 6(c)]. This again, is as expected for an incompressible 1/3 FCI state [64].

While a 1/3 FCI state in a single layer kagome system has been reported earlier, for example in Ref. [64], our results in Fig. 6 show that such a FCI state is stable even in the *bilayer* system in the presence of interlayer hybridization ($t_{\perp}$) and appreciable interlayer repulsion ($V_{\perp}$).

2. **1/5** *fractional Chern insulator*

We now investigate the effect of nearest-neighbor repulsion on the Chern metallic phase, in the strong hybridization limit with the Fermi energy in the $C = 2$ band, shown in Fig. 5(b). Remarkably, at 1/5 filling of this band, within the exact diagonalization scheme discussed above, we realize a 1/5 FCI state. With periodic boundary conditions, this FCI phase is characterized by a five fold quasidegenerate ground state manifold [see Fig. 7(a)], which is clearly separated from the excited states by a gap that does not change significantly over the few system sizes, 5×5, 5×6, and 5×7, that we could explore. Two additional features in Fig. 7(a) are conspicuous: (1) the total momenta of the states in the ground state manifold for every system size that we study agrees with the prediction of the generalized Pauli principle (see Appendix D). (2) The ground state manifold itself exhibits a relatively large splitting between a unique "ground" state and the other four states. While the first feature is a strong evidence in the favor of a 1/5 FCI phase the second feature may raise doubts about its stability. The concern about the stability of the 1/5 FCI phase is further supported by the data presented in Fig. 7(b) for the 5×6 system. This figure shows the average density of the electrons in a single particle Bloch

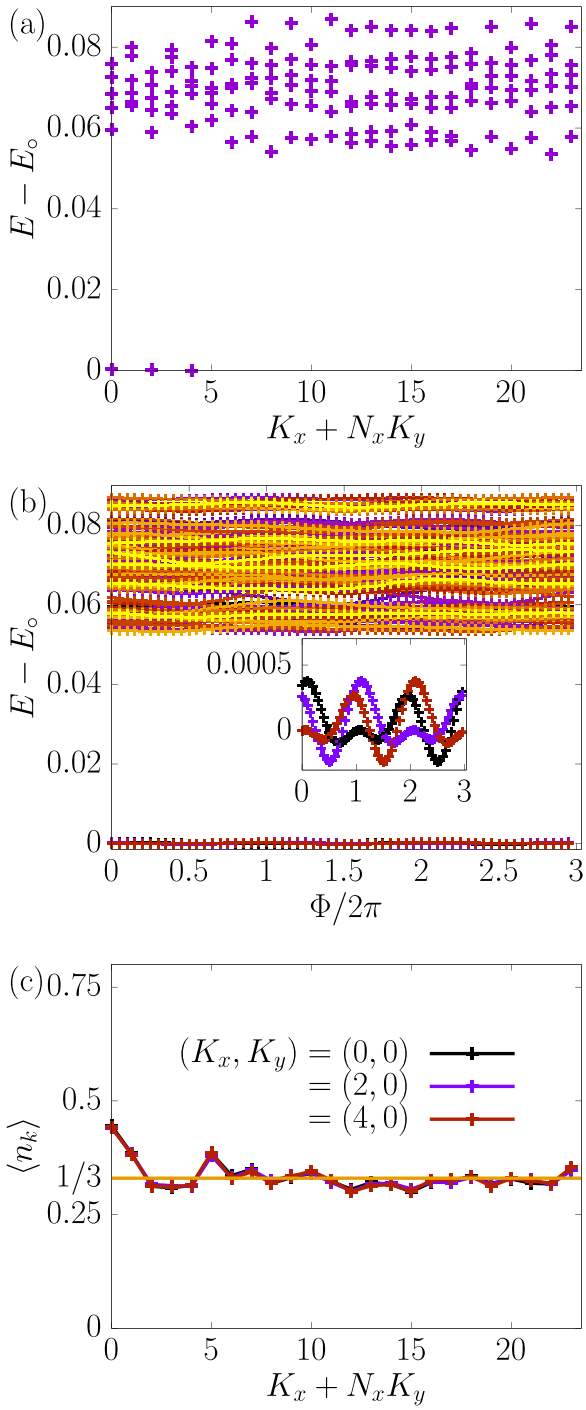

FIG. 6. *1/3 FCI state.* (a) Low-energy spectra for the 1/3 state on a 6×4 periodic boundary system for the bands in Fig. 5(a) showing a threefold degenerate ground state. (b) Flux threading results for the 1/3 state showing that the ground state manifold remains gapped while exhibiting a periodicity of $\Phi = 6\pi$. Different colors are used to distinguish the total momenta of the states. (c) $\langle n(k) \rangle \sim 1/3$ for all values of k in the three ground states.

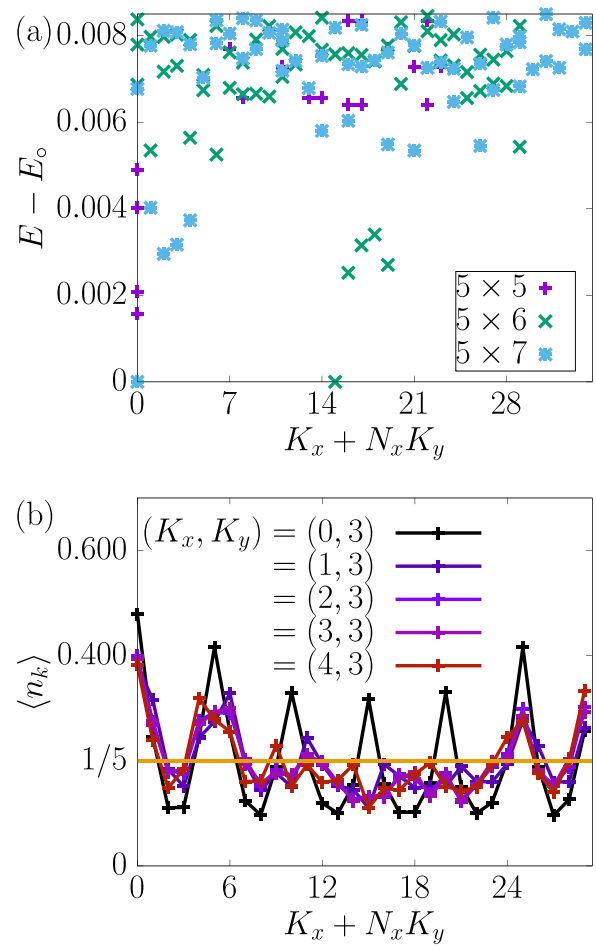

FIG. 7. *1/5 FCI state.* (a) Low-energy spectra for the 1/5 state with periodic boundary system for the band in Fig. 5(b) showing a fivefold quasidegenerate ground state manifold for different system sizes. (b) $\langle n(\mathbf{k}) \rangle \sim 1/5$ for all $\mathbf{k}$ in the five quasidegenerate ground states for the 5×6 system.

state having Bloch momentum $\mathbf{k}$ in the band at the Fermi energy, $\langle n_\mathbf{k} \rangle$, for all the five states in the ground state manifold. While four of the states show $\langle n(k) \rangle \sim 1/5$, the lowest energy state with $(K_x, K_y) = (0, 3)$ exhibits a distinctive oscillation over the mean density of 1/5 and thus, indicates the breaking of additional rotational symmetries of the thermodynamic system.

We believe, however, that this breaking of rotational symmetry of the thermodynamic system is an artifact of the missing rotational symmetries in our finite size system in the first place. Note that our exact diagonalization studies are performed in the momentum basis. The smallest momentum grid which would have all the rotational symmetries of the thermodynamic system and can simultaneously have a filling of 1/5 is 15 × 15 with 45 particles. This is well beyond our computational capacity and consequently the systems sizes that we study are far from this symmetric point. It is useful to contrast this with the case for the 1/3 FCI phase. In that case, the two smallest systems which had all the rotational symmetries of the thermodynamic system were 3 × 3 with 3 particles and 6 × 6 with 12 particles. While 3 × 3 was too small for any reliable conclusion, the system size that we studied, 6 × 4 with 8 particles was not very far from the 6 × 6 system. Therefore the splitting in the ground state manifold for the 1/3 FCI state was not as pronounced as in the 1/5 case.

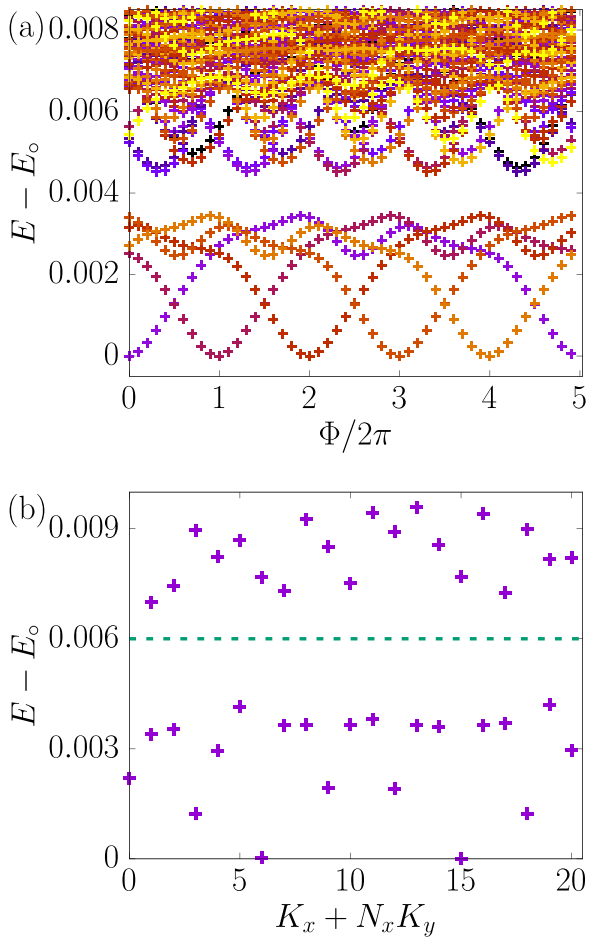

FIG. 8. *Additional evidence of 1/5 FCI state.* (a) Flux threading results for the 1/5 state on a 5×6 momentum space grid showing that the ground state manifold remains gapped while exhibiting a periodicity of $\Phi = 10\pi$. Different colors are used to distinguish the total momenta of the states. (b) The many-body spectrum for the flattened $C = 2$ band in Fig. 5(b) with one quasihole about the 1/5 FCI state, calculated for 3×7 system with four particles. The low-energy states, below the dashed line, follow the expected generalized Pauli principle (see Appendix D for details).

Despite the difficulty with the accessible system sizes resulting in the artificial charge oscillations in Fig. 7(b), there are a couple of additional evidences that strongly suggest that the bilayer kagome system is indeed capable of realizing a 1/5 FCI phase. (1) With twisted boundary conditions where an additional flux Φ is introduced, one finds that the five states in the ground state manifold remain isolated from the excited states while exhibiting a twist angle periodicity of 10π [see Fig. 8(a)]. This is a rather compelling evidence of the nontrivial topological character of the lowest five states and thus, is a strong evidence in favor of a 1/5 FCI phase. (2) The quasihole spectrum, presented in Fig. 8(b), also follows the generalized Pauli principle (see Refs. [64,70,71] and Appendix D) which makes it further convincing that the lowest five many-body states in the spectrum in Fig. 7(a) indeed form a 1/5 FCI quasidegenerate ground state manifold.

It is worth noting that the 1/5 FCI state that we uncover for the bilayer kagome system is reminiscent of a similar state which was found for pyrochlore slabs that also inherits the kagome motifs [63]. We also note that for a $C = 2$ tight-binding band which closely resembles the band at the Fermi energy for the bilayer Fe_3Sn_2 as obtained from the first principles, we do not find a FCI state for the system sizes that we could access.

IV. INSTABILITIES OF THE NONMAGNETIC PHASE

Having discussed the phases in the vicinity of the Chern metal, we now turn to the case where the quantum fluctuations in the bilayer kagome, owing to its low dimensionality, are strong enough to destabilize the ferromagnetic order. The resultant nonmagnetic metal is best described by the time reversal symmetric hopping Hamiltonian in Eq. (1) along with the short-range interactions in Eq. (3). Taking cue from the first principles, which predicts a large density of states at and close to the Fermi energy owing to the presence of several nearly flat bands (see Fig. 3(c) of Ref. [51]), we propose to work with a set of hopping parameters provided in Fig. 4 which captures this band phenomenology adequately. In the rest of this section, we shall discuss the effect of the short-range interactions over these tight-binding bands at appropriate fillings, while highlighting some of the interesting instabilities of the nonmagnetic phase.

In the limit of large onsite repulsion and at electron densities of less than one per site, we can restrict to a space of electronic states which have no double occupancies. An appropriate parton paradigm in this limit splits the electron creation operator ($c^\dagger_{i\sigma}$) into a fermionic spinon creation operator ($f^\dagger_{i\sigma}$) and a bosonic hole annihilation operator (b_i) such that

$$c^\dagger_{i\sigma} = f^\dagger_{i\sigma} b_i \tag{6}$$

with a local constraint

$$\sum_\sigma f^\dagger_{i\sigma} f_{i\sigma} + b^\dagger_i b_i = 1 \quad \forall\, i. \tag{7}$$

Clearly, Eq. (6) leads to a U(1) gauge redundancy with the spinons and the holons carrying a unit charge each with respect to the corresponding gauge field [72]. This U(1) gauge structure is in addition to the one associated with electromagnetism; the source of the interaction terms in Eq. (3). To avoid any possible confusion we refer to the gauge structure implied by Eq. (6) as the internal gauge structure. Furthermore, it is easy to convince oneself that within this parton construction the number of spinons at any given site must be identified with the number of electrons at that site, while the number of holons gives the probability of the site being empty.

A. *t-J-V* model

A natural model to work with is an appropriate *t-J-V* model [73] defined in the no-double-occupancy sector of the electronic Hilbert space. In the presence of nearest-neighbor interactions (V_{ij}) which are sub-dominant to the onsite interaction (U), this model Hamiltonian takes the following

form:

$$H_{tJV} = -\sum_{\substack{ij\\ \sigma,\sigma'}} t_{ij}^{\sigma\sigma'} c_{i\sigma}^{\dagger} c_{j\sigma'} - \mu \sum_i n_i + \sum_{\langle ij\rangle} \left[J_{ij} \boldsymbol{S}_i \cdot \boldsymbol{S}_j + \left(V_{ij} - \frac{J_{ij}}{4} \right) n_i n_j \right], \tag{8}$$

where $S_i^{(\tau)} = \frac{1}{2} \sum_{ss'} c_{is}^{\dagger} \sigma_{ss'}^{(\tau)} c_{is'}$ with $\sigma^{(\tau)}$ being the Pauli matrices and $n_i = \sum_{\sigma} c_{i\sigma}^{\dagger} c_{i\sigma}$ are, respectively, the electronic spin and number operators at site i. $t_{ij}^{\sigma\sigma'}$ are the same as in Eq. (1) with values provided in Fig. 4 and μ is the chemical potential. J_{ij} is the strength of the nearest-neighbor anti-ferromagnetic exchange interaction that one obtains in the usual derivation of the t-J model (see, for example, Refs. [74,75]). Note that in Eq. (8), we are not including the exchange processes arising from next nearest neighbor hopping or from the effective spin-orbit coupling as their contribution ($\sim g^2/U$, where g is the amplitude of the hopping process) is much smaller compared to that from the nearest-neighbor hopping processes.

For the purpose of highlighting qualitatively nontrivial physics, we find it sufficient to set $J_{ij} = J$ and $V_{ij} = V$ for all the nearest-neighbor site indices i and j. With these simplifications H_{tJV} can be rewritten in a suggestive form as

$$H_{tJV} = \sum_{ij} t_{ij}^{\sigma\sigma'} c_{i\sigma}^{\dagger} c_{j\sigma'} - \tilde{\mu} \sum_i n_i - J_{\Delta} \sum_{\langle ij\rangle} B_{ij}^{\dagger} B_{ij} - J_{\kappa} \sum_{\langle ij\rangle} K_{ij}^{\dagger} K_{ij}, \tag{9}$$

where $\tilde{\mu} = \mu - V$ is the renormalized chemical potential, $J_{\Delta} = J - 2V$ and $J_{\kappa} = 2V$. $B_{ij}^{\dagger} = (c_{i\uparrow}^{\dagger} c_{j\downarrow}^{\dagger} - c_{i\downarrow}^{\dagger} c_{j\uparrow}^{\dagger})/\sqrt{2}$ is the creation operator for a two electron singlet with one sitting on the i-th site and another on the jth site, while $K_{ij}^{\dagger} = (c_{i\uparrow}^{\dagger} c_{j\uparrow} + c_{i\downarrow}^{\dagger} c_{j\downarrow})/\sqrt{2}$ is an operator which facilitates the hopping of an electron from site j to site i. Clearly, if $J_{\Delta} > 0$, that is $J > 2V$, a superconducting ground state is plausible at any electron filling of less than one electron per site. Conversely, if $J_{\Delta} < 0$, one would obtain a correlated metal. For $J_{\Delta} \sim 0$ one expects a quantum critical phase dominated by long-wavelength fluctuations of the superconducting order parameter over a metallic background.

Before diving deeper into the nature of the superconducting phase supported by H_{tJV}, we must note that our original t-U-V model [see Eqs. (1) and (3)], just like the repulsive Hubbard (t-U) model, has no well-accepted evidence for a superconducting phase. However, the conventional t-J model derived from the repulsive t-U model does show signatures of superconductivity (see, for example, Ref. [76]). Similarly, the t-J-V model, for small values of V/t does indeed support superconductivity (see, for example, Ref. [77]). In the following sections, we describe a superconducting phase of H_{tJV} and its zero temperature transition to a metallic phase within the parton paradigm discussed above. It is easy to convince oneself that the J_{Δ} and J_{κ} terms in Eq. (9) have the same matrix elements in the electronic basis and in the spinonic basis even while leaving out the holon operators [72]. Therefore, for the purpose of streamlining, the analysis that follows we shall write them completely in terms of the spinon operators. Moreover, in our analysis, we shall relax the local constraints Eq. (7) to a global constraint with the understanding that the physical wave functions can be obtained by projecting our wave functions to the space of physical states [78,79].

1. High-T_c superconductivity

For a generic electron density $(1 - p)$ of less than one electron per site, the holons can safely be assumed to condense into a superfluid state with $\langle b_i \rangle \sim \sqrt{p}$. This results in a renormalization of the hopping amplitudes for the electronic quasiparticles, $t_{ij}^{\sigma\sigma'} \to p t_{ij}^{\sigma\sigma'}$ and thus captures the correct behavior in the two limiting cases of $p \to 0$ where one expects a Mott insulating ground state, and $p \to 1$ where one expects a Fermi liquid ground state. The condensation of holons further gaps out the internal gauge fields via the Anderson-Higgs mechanism and, by appropriately redefining the spinonic operators, allows us to work with electron-like operators [80]. In this background of condensed holons, we then obtain a mean-field Hamiltonian H_{tJV}^{MF} via the decomposition of the quartic terms in Eq. (9) in the pairing ($\{\Delta_{ij}\}$) and the kinetic channels ($\{\chi_{ij}\}$)

$$J_{\Delta} B_{ij}^{\dagger} B_{ij} \simeq \Delta_{ij}^{*} B_{ij} + B_{ij}^{\dagger} \Delta_{ij} - \frac{|\Delta_{ij}|^2}{J_{\Delta}}, \tag{10}$$

$$J_{\kappa} K_{ij}^{\dagger} K_{ij} \simeq \chi_{ij}^{*} K_{ij} + K_{ij}^{\dagger} \chi_{ij} - \frac{|\chi_{ij}|^2}{J_{\kappa}}. \tag{11}$$

Finally, to solve H_{tJV}^{MF} self-consistently, we impose

$$\Delta_{ij} = J_{\Delta} \langle B_{ij} \rangle_{\mathrm{MF}}, \tag{12}$$

$$\chi_{ij} = J_{\kappa} \langle K_{ij} \rangle_{\mathrm{MF}}, \tag{13}$$

where $\langle\ \rangle_{\mathrm{MF}}$ denotes that the expectation value is being computed in the ground state of H_{tJV}^{MF}. We also simultaneously adjust the chemical potential to accommodate p electrons per site on an average.

Let us first discuss the superconducting phase that we obtain in the limit of vanishing nearest-neighbor repulsion V at $T = 0$ K. In this limit, Eqs. (11) and (13) can be dropped, while $1/3 < p < 2/3$ is such that the noninteracting Fermi surface lies in the flat band (see Fig. 4). The eighteen superconducting order parameters $\{\Delta_{ij}\}$ associated with a unit cell live on the bonds of the lattice [see Fig. 9(c)] and can be divided into three disjoint sets on the basis of their transformation properties under the lattice symmetries. The bonds in any one of these sets mix under the lattice symmetries and thus, host superconducting order parameters of the same magnitude. The maximum magnitude of the pairing order parameter among these three sets, which should eventually decide the superconducting transition temperature, is defined to be $|\Delta|_{\max}$ ($|\chi|_{\max}$ is defined analogously).

$|\Delta|_{\max}/t$ as a functions of p has a dome shape with a vanishing trend close to the band edges $p = 1/3$ and $2/3$ where the electronic density of states vanish. We show this in Fig. 9(a) for $J/t = 1/2$ and $1/4$. In Fig. 9(b), we plot $\{\Delta_{ij}\}$ over the lattice, with the thickness of the bond between sites i and j being proportional to the magnitude of Δ_{ij} and its phase being coded in the color of the bond. Clearly, the intralayer and interlayer pairing order parameters are out of phase while being invariant under lattice rotations, suggesting an $s_{\pm}$-wave symmetry of the pair wave function. In terms of absolute

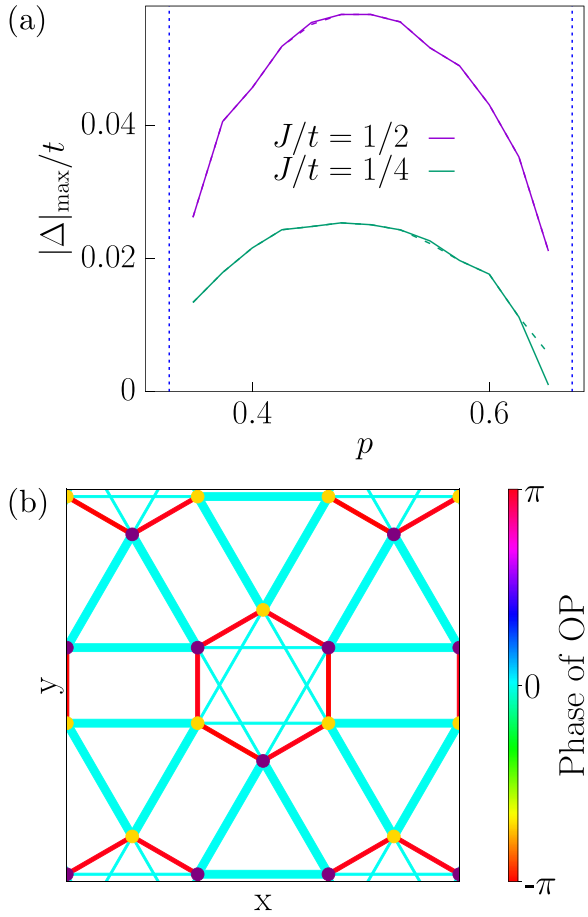

FIG. 9. *SC within t-J-V model.* (a) Behavior of $|\Delta|_{\max}/t$ as a function of p for $J/t = 1/2$ and $1/4$, obtained by solving t-J model in $V = 0$ limit. Solid (dashed) curves correspond to results obtained with a momentum space mesh of 151×151 (101×101) and the blue dotted lines mark the band edges at $p = 1/3$ and $2/3$. (b) Corresponding real space variation of the superconducting order parameter at $J/t = 1/4$ and $p = 0.5$. The width of the bonds represent the magnitude of Δ (maximum $\sim 0.025t$ and and minimum $\sim 0.007t$) while the phase has been color coded.

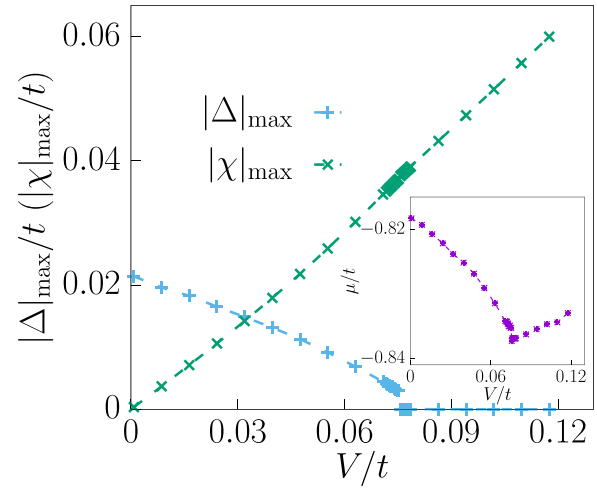

FIG. 10. *SC to metal transition as a function of V/t.* Behavior of $|\Delta|_{\max}/t$ and $|\chi|_{\max}/t$ as a function of the nearest-neighbor repulsion V/t at $J/t = 0.25$ and $p = 0.4$. The inset shows the chemical potential as V/t is tunned across the superconductor to metal transition at $V_c \lesssim J/2$. The momentum space mesh grid used for this calculation was 151×151.

energy scales for $t \sim 0.1$ eV, $J \sim 0.05$ eV, and $p = 0.5$, we find a $|\Delta|_{\max}$ of the order 5%–6% of t which corresponds to a maximum $T_c \sim \langle b_i^\dagger b_j^\dagger \rangle |\Delta|_{\max} \sim p|\Delta|_{\max}$ of about 30–35 K, which is rather high given that we are significantly away from a filling of one electron per site.

2. Correlated metal

The superconducting state that we obtained above seems quite robust and can in principle be the dominant instability of the nonmagnetic metal in the bilayer kagome system. However, if this superconducting phase could be suppressed some even more exotic phases might become realizable. Extensions of the Lieb-Schultz-Mattis theorem [81] suggest that at a filling of 3 electrons per unit cell ($p = 0.5$) if the electron-electron interactions are unable to stabilize an ordered phase with a broken symmetry then a quantum spin liquid ground state is possible. At this filling, the band at the Fermi energy in Fig. 4 is half filled and the corresponding Wannier orbitals would form a triangular lattice. On incorporating the effect of microscopic interactions appropriately one expects to obtain an effective tight-binding model with one orbital per site and some short-ranged interactions on the triangular lattice. The triangular lattice, like the kagome lattice, is prone to frustrations and hence can be expected to host one of the exotic quantum spin liquid phases (see, for example, Ref. [53]). Thus it is pertinent to discuss the possible mechanisms of suppressing the superconducting order.

A mechanism for this suppression is provided by the fluctuations of the collective excitations about the superconducting state [82] which may leave us with a correlated nonmagnetic metal. Increasing the nearest-neighbor interaction strength V offers yet another natural pathway for the suppression of the superconducting order in the bilayer kagome systems. Figure 10 shows the results of our mean-field calculations for H_{tJV} in Eq. (9) with nonzero values of V at $J/t = 0.25$ and $p = 0.4$. We find that as V is increased towards $J/2$ the superconducting order parameter decreases monotonically and eventually vanishes via a first-order quantum phase transition when $V_c \lesssim J/2$ to become a correlated metal as V/t is increased further. A more detailed study uncovering the interesting instabilities, including ordering by symmetry breaking, of this correlated metal remain an interesting direction for future work.

V. SUMMARY AND DISCUSSION

Kagome intermetallics are an interesting set of materials which offers an ideal playground for studying the interplay of topology and strong correlation effect. Motivated by the rich physics offered by M_3Sn_2 class of these compounds, and possible experimental synthesis of bilayers of these materials, in this work, we investigate the correlation driven instabilities in the kagome bilayer systems. Employing appropriate numerical and analytical tools we solve the material-inspired model Hamiltonian. We consider the two starting states, (a) a Chern

metal with spin-polarized bands and (b) a nonmagnetic metallic phase with magnetism being destroyed due to enhanced fluctuations in two dimensions. We discover correlation-driven instabilities towards exotic phases, like fractional chern insulator, superconductivity and correlated metal.

Turning on the correlation effect on Chern metallic phase, our analysis unravels possibility of two different FCI states. In the weak interlayer hybridization limit with the system hosting a flat band of Chern number $C = 1$ near the Fermi energy, at one-third filling appears to stabilize a $1/3$ FCI state, while in the limit of strong interlayer hybridization where the system hosts a flat band with $C = 2$ at the Fermi energy a $1/5$ FCI state may get stabilized. The gap to excitations in the $1/3$ and $1/5$ FCI states are estimated to be $\sim$0.02 and 0.002 V, respectively, (see Figs. 6 and 7), where V is the intersite interaction strength. Assuming a $V \sim 0.5$ eV, this would correspond to the gap scale of $\Delta_{1/3}^{\mathrm{FCI}} \sim 10$ meV for the $1/3$ FCI and $\Delta_{1/5}^{\mathrm{FCI}} \sim 1$ meV for the $1/5$ FCI, which are comparable to the width of the flat band in the bilayer kagome compound as predicted from first-principles calculations [51]. This suggests that to achieve the observed FCI states in the real materials, further band engineering may be needed to flatten out the bands at the Fermi energy. Also the separation of flat bands need to be ensured, demanding experimenting with choice of substrate, gating and strain engineering.

Consideration of strong repulsive interaction in the nonmagnetic situation, with restored time-reversal symmetry, leads to distinctly different scenario. Here, using the appropriate t-J-V model, we show that the system can realize a superconducting phase akin to high-temperature superconducting phases. Interestingly this superconducting phase undergoes a transition to a correlated metal as the intersite repulsive interaction is increased. This further opens up the possibility of realizing a quantum spin liquid phase when the band at the Fermi energy is half filled. The precise nature of the superconductor to the correlated metal transition, beyond mean-field approximation, and similarly the character and the instabilities of the correlated metal are interesting directions for future work.

It is important to note that in our work, we have considered only the effect of repulsive interaction. As shown in Ref. [51], an attractive interaction in Chern metallic phase can lead to a topological superconducting phase. This might have phononic origins as has recently been seen in some transport experiments in antimony based compounds [83]. Out of the several possible instabilities, which one will dominate will depend upon the material specific details of the band structure, the strength and nature of the short-ranged electron-electron correlation and electron-phonon interactions. Tuning mechanisms available due to the layered and cleavable nature of the systems, though, make the situation promising, opening up the door for experimental exploration. Using the substrate effect, straining and gating as handles we envisage a rich phase diagram to emerge in this class of compounds.

ACKNOWLEDGMENTS

We acknowledge S. Bhattacharjee for extensive discussions related to this work and collaborations on related projects and ideas. We acknowledge use of open-source QUSPIN [84,85] for exact diagonalization calculations. A.A. acknowledges support from IITK Initiation Grant (IITK/PHY/2022010). We acknowledge the hospitality of International Centre for Theoretical Sciences (ICTS), Bengaluru where a significant part of this work was done. During this time A.V.M. was also supported by a postdoctoral fellowship of ICTS, Bengaluru. T.S.-D. acknowledges J.C. Bose National Fellowship (Grant No. JCB/2020/000004) for funding.

TABLE I. Symmetry analysis. This table shows how different real space (1, 2, 3, 1′, 2′, and 3′ are the sites in a unit cell; see Fig. 1) and reciprocal space (Γ, K, K', M, M', and M'' are high symmetry points in the hexagonal Brillouin zone; see inset of Fig. 4) degrees of freedom (dof's) transform under a representative element of each of the conjugacy classes of the D_{3d} point group (see, for example, Ref. [86]).

dof's	E	C_3	C_2'	i	S_6	σ_d
1	1	2	1′	1′	3′	1
2	2	3	3′	2′	1′	3
3	3	1	2′	3′	2′	2
1′	1′	2′	1	1	3	1′
2′	2′	3′	3	2	1	3′
3′	3′	1′	2	3	2	2′
Γ	Γ	Γ	Γ	Γ	Γ	Γ
K	K	K	K	K'	K'	K'
K'	K'	K'	K'	K	K	K
M	M	M''	M	M	M'	M
M'	M'	M	M''	M'	M''	M''
M''	M''	M'	M'	M''	M	M'

APPENDIX A: LOW-ENERGY TIGHT-BINDING MODELS

The point group symmetry of the bilayer kagome lattice (see Fig. 1) is D_{3d} (see Table I). Given that the spin dependent hopping in Eq. (2) does not mix the spin flavors we can still use $S_z = \uparrow, \downarrow$ as a good quantum number.

Here, we present the symmetry analysis of the bands for both $\lambda = 0$ and $\lambda \neq 0$ separately for the tight-binding Hamiltonians. When $\lambda = 0$, the little group at the Γ point of Brillouin zone is D_{3d}. From Table I, one finds the reducible character vector of this group representation R_Γ to be (6, 0, 0, 0, 0, 2) which implies $R_\Gamma = A_{1g} \bigoplus E_g \bigoplus A_{2u} \bigoplus E_u$ implying two nondegenerate and two doubly degenerate states at the Γ point. The little group of the K point includes the transformations C_3 and C_2' which generate the discrete group D_3 (see Ref. [86]). The corresponding transformation matrices can be read off from Table I and they together form a representation R_K of D_3. The character vector for R_K turns out to be (6,0,0) implying that $R_K = A_1 \bigoplus A_2 \bigoplus 2E$. Therefore the degeneracies in the spectrum at the K point is exactly the same as that at the Γ point discussed above. The little group of the M point is the Abelian group C_i and its reducible representation given in Table I R_M, has (6,0) as its character vector. Consequently, the spectrum at the M point is nondegenerate with $R_M = 3A_g \bigoplus 3A_u$.

For $\lambda \neq 0$, the point group symmetry of each spin sector changes from D_{3d} to S_6 which only has one dimensional irreducible representations (see Ref. [86]). The character

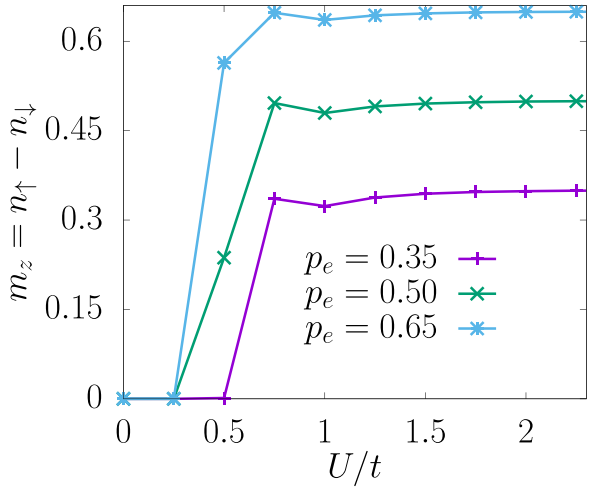

FIG. 11. *Mean-field ferromagnetism.* For the bands presented in Fig. 4, we plot the average magnetization per site ($m_z = 1/N_s \sum_i (n_{i\uparrow} - n_{i\downarrow})$) against the strength of onsite Hubbard interaction U/t for different values of electron filling per site p_e [$V_{ij} = 0$, see Eq. (3)]. Fully spin polarized state is realized for $U/t \gtrsim 1.0$.

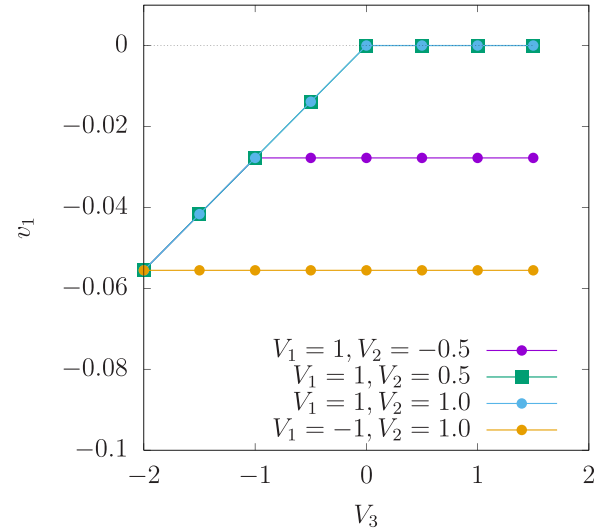

FIG. 12. *Absence of SC in Chern metal.* Variation of v_1 ($= \{v_n\}_{\min}$) for some representative values of V_1, V_2, and V_3, showing that when $V_1, V_2, V_3 > 0$ the system does not host any $v_n < 0$.

vector of this representation at the Γ point is (6,0,0,0,0,0) (see Table I) which means a completely nondegenerate spectrum. Similarly, the little group at the K point is C_3 (see Ref. [86]) which admits only one dimensional irreps, implying a nondegenerate spectrum, with each irrep appearing twice.

The change in the dimension of the irreps in the presence of λ as compared to those in its absence is evident from the dispersion at the Γ and the K points as shown in Fig. 4. We note that the bands at every momentum point has an additional two-fold degeneracy, which is guaranteed by a combination of time reversal and inversion.

The inversion symmetry, however, may generally be absent in an experimental realization because of the presence of a substrate or an applied gate potential. When $\lambda = 0$, the residual point group symmetry of a given S_z sector is C_{3v} (see, for example, Ref. [86]). The reducible representation (see Table I) at the Γ, has the character vector (6,0,2), implying the following decomposition in terms of the irreducible representations of C_{3v}, $2A_1 \bigoplus 2E$. The little groups at the K and the M points are, respectively, C_3 and C_1, which are both Abelian. When $\lambda \neq 0$, the point group symmetry of the system reduces to C_3 implying generically nondegenerate bands at all momenta in the Brillouin zone. When both the S_z sectors are considered such that time-reversal T with $T^2 = -\mathbb{1}$ is also present, the band structure exhibits Kramer's degeneracy.

APPENDIX B: MEAN-FIELD FERROMAGNETISM

A self-consistent mean-field analysis of the onsite repulsive term [see Eq. (4)] for the free dispersion given in Fig. 4 results in fully spin-polarized band at low energies for $U/t \gtrsim 1$ (see Fig. 11).

APPENDIX C: ABSENCE OF SUPERCONDUCTIVITY WITH REPULSIVE INTERACTIONS FOR CHERN METAL

The quartic term in a many body Hamiltonian which describes the scattering of two fermion pairs, each with a zero center-of-mass momentum, is relevant for the formation of Cooper pairs. The zero-momentum scattering term is given by

$$H_p = \sum_{\substack{k,k' \\ s_1,s_2,s_3,s_4}} V_{k,s_1,s_2;k',s_3,s_4} c^\dagger_{ks_1} c^\dagger_{-ks_2} c_{-k's_4} c_{k's_3}, \qquad \text{(C1)}$$

where k and k' are momentum indices, $s_{1(234)}$ denote both the atomic sites within the unit cell and also the spins. $V_{k,s_1,s_2;k',s_3,s_4}$, owing to fermionic statistics, satisfies $V_{k,s_1,s_2;k',s_3,s_4} = -V_{-k,s_2,s_1;k',s_3,s_4} = -V_{k,s_1,s_2;-k',s_4,s_3} = V_{-k,s_2,s_1;-k',s_4,s_3}$. Whether a zero-momentum pairing in any

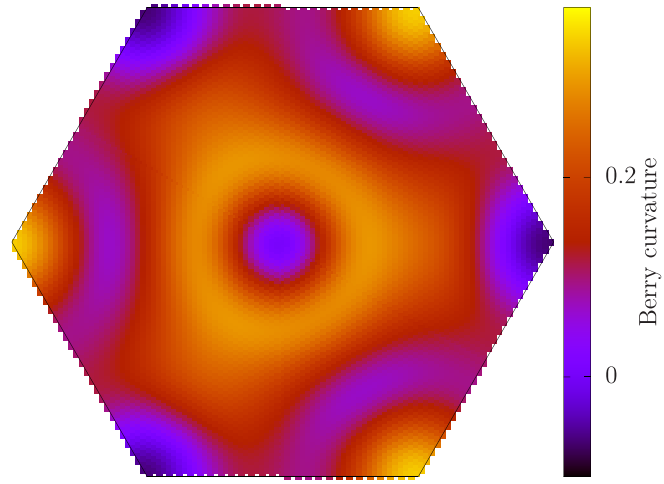

FIG. 13. *Berry curvature.* Berry curvature distribution over the hexagonal Brillouin zone for the $C = 1$ band at the Fermi energy in Fig. 5(a).

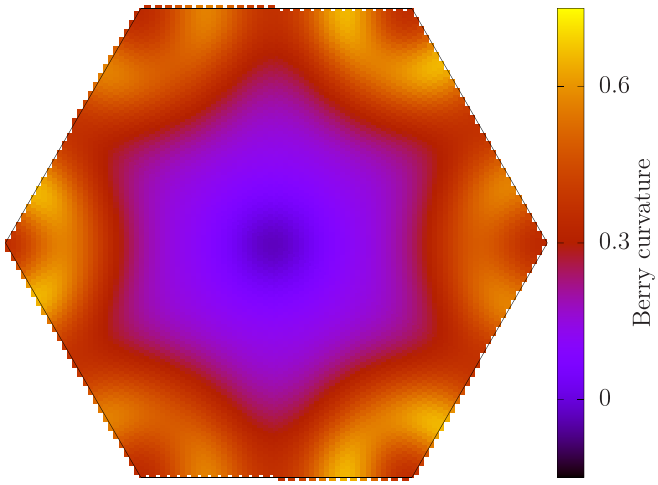

FIG. 14. *Berry curvature*. Berry curvature distribution over the hexagonal Brillouin zone for the $C = 2$ band at the Fermi energy in Fig. 5(b).

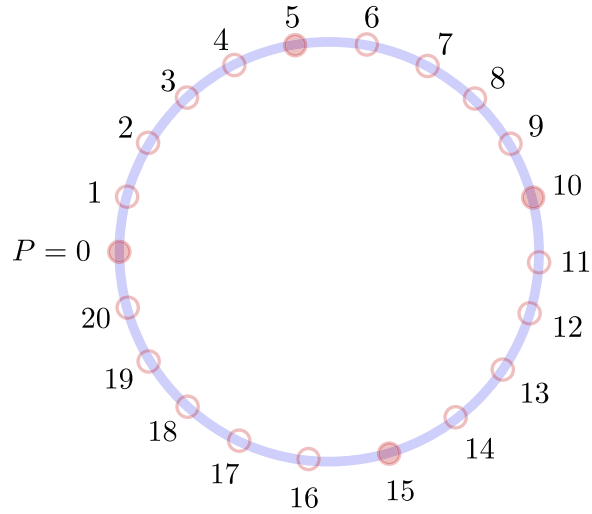

FIG. 15. *Degeneracy and momenta of quasihole states in Fig. 8.* The figure shows a classical ground state configuration for $N_x \times N_y = 3 \times 7$ system with $N_p = 4$ particles when mapped to the ring (see Appendix D for details). Each pink circle corresponds to a unique single particle Bloch state in the first Brillouin zone of the lattice problem ($P = K_x + N_x K_y$) and a filled circle represents occupation by a particle. For the shown configuration, the total Bloch momentum of the quasihole state is $(K_x, K_y) = (0, 2)$. A new configuration corresponding to another state in the low-energy manifold in Fig. 8 can be generated by increasing the index (P) of each particle by 1. This can be repeated to generate configurations corresponding to all the 21 states in the low-energy manifold of the quasihole spectrum presented in Fig. 8.

angular-momentum channel is favored can be found by rewriting Eq. (C1) as

$$H_p = \sum_{\substack{k,k' \\ s_1,s_2,s_3,s_4}} c^\dagger_{ks_1} c^\dagger_{-ks_2} V_{k,s_1,s_2;k',s_3,s_4} c_{-k's_4} c_{k's_3}$$
$$\equiv \sum_n v_n \hat{\Delta}^\dagger_n \hat{\Delta}_n, \tag{C2}$$

where v_n is nth eigenvalue of matrix V. The numbers $\{v_n\}$ denote the bound state energies of the n^{th} zero momentum fermion pair where Δ_n is given by

$$\hat{\Delta}_n = \sum_{k',s_3,s_4} \mathrm{U}^\dagger_{n;k',s_3,s_4} c_{-k's_4} c_{k's_3}, \tag{C3}$$

such that U diagonalizes Eq. (C2). Under a self-consistent Hartree-Fock, different pairing amplitudes Δ_n may take a finite expectation value. When the Fermi surface is nearly circular a superconducting instability in the nth channel is expected if $v_n < 0$ [87,88].

When such an analysis is performed for the ferromagnetic Chern metallic band, for three kinds of repulsive interactions: (i) V_1: Intralayer intra-unit-cell nearest-neighbor density-density interaction, (ii) V_2: Intralayer inter-unit-cell nearest-neighbor density-density interaction, and (iii) V_3: Interlayer intra-unit-cell nearest-neighbor density-density interaction, we find no window in the parameter space for $(V_1, V_2, V_3 > 0)$ when $v_n < 0$ signaling a BCS state cannot be realized within a self-consistent mean-field theory for purely repulsive microscopic interactions. Variation of v_1 $(= \{v_n\}_{\min})$ for some representative values of V_1, V_2 and V_3 is shown in Fig. 12.

APPENDIX D: FRACTIONAL CHERN INSULATOR

Here we present additional results pertaining to the FCI states.

FCI 1/3. The Berry curvature over the hexagonal Brillouin zone for the $C = 1$ band at the Fermi energy in Fig. 5(a) is shown in Fig. 13.

FCI 1/5. The Berry curvature over the hexagonal Brillouin zone for the $C = 2$ band at the Fermi energy in Fig. 5(b) is shown in Fig. 14.

The generalized Pauli principle for FCI phases. The number of topological (quasi)degenerate zero modes in the many-body spectrum of a FCI phase and their respective Bloch momentum can be obtained by an intricate mapping of the lattice problem to an appropriate multicomponent continuum quantum Hall system and then considering its thin torus limit [71]. Eventually, one ends up solving a classical electrostatics problem defined on a ring with $N_x N_y$ lattice sites and N_p particles which repel each other by a pairwise interaction decaying with the distance (along the ring) between them. The sites on the ring are placed at an equal angular spacing of $2\pi/N_x N_y$ and are labeled by an index $P \in \{0, 1, \ldots, N_x N_y - 1\}$ such that every site on the ring is uniquely mapped to a Bloch momentum $(k_x = 2\pi K_x/N_x, k_y = 2\pi K_y/N_y)$ via $P = K_x + N_x K_y$. The number of topological (quasi)degenerate zero modes in the lattice problem is then equal to the number of lowest energy (classical) configurations of the N_p mutually repelling particles on the ring and the corresponding Bloch momentum is just the sum of the Bloch momenta of the individual particles in that configuration. Some deviations from this prescription are possible and have been discussed in detail in Ref. [71].

It is straight forward to verify that this procedure does correctly predict the degeneracy and the momenta of each state in the low-energy quasidegenerate manifold of the 1/3 and 1/5 FCI states presented in Figs. 6(a) and 7(a). Moreover, it also predicts the degeneracy and the momenta of each of the 1/5 FCI quasihole states in the low-energy manifold of the spectrum presented in Fig. 8. In this case, there is exactly one state at each Bloch momentum point (see Fig. 15).

[1] M. Z. Hasan and C. L. Kane, *Colloquium* : Topological insulators, Rev. Mod. Phys. **82**, 3045 (2010).

[2] C.-K. Chiu, J. C. Y. Teo, A. P. Schnyder, and S. Ryu, Classification of topological quantum matter with symmetries, Rev. Mod. Phys. **88**, 035005 (2016).

[3] A. W. W. Ludwig, Topological phases: Classification of topological insulators and superconductors of non-interacting fermions, and beyond, Phys. Scr. **2016**, 014001 (2016).

[4] X.-L. Qi and S.-C. Zhang, Topological insulators and superconductors, Rev. Mod. Phys. **83**, 1057 (2011).

[5] F. D. M. Haldane, Model for a quantum Hall effect without Landau levels: Condensed-matter realization of the "parity anomaly", Phys. Rev. Lett. **61**, 2015 (1988).

[6] C. L. Kane and E. J. Mele, Quantum spin Hall effect in graphene, Phys. Rev. Lett. **95**, 226801 (2005).

[7] J. K. Jain, *Composite Fermions* (Cambridge University Press, Cambridge, England, 2007).

[8] T. H. Hansson, M. Hermanns, S. H. Simon, and S. F. Viefers, Quantum Hall physics: Hierarchies and conformal field theory techniques, Rev. Mod. Phys. **89**, 025005 (2017).

[9] G. Murthy and R. Shankar, Hamiltonian theories of the fractional quantum Hall effect, Rev. Mod. Phys. **75**, 1101 (2003).

[10] R. Bistritzer and A. H. MacDonald, Moiré bands in twisted double-layer graphene, Proc. Natl. Acad. Sci. **108**, 12233 (2011).

[11] Y. Cao, V. Fatemi, S. Fang, K. Watanabe, T. Taniguchi, E. Kaxiras, and P. Jarillo-Herrero, Unconventional superconductivity in magic-angle graphene superlattices, Nature (London) **556**, 43 (2018).

[12] G. L. Caer, B. Malaman, and B. Roques, Mossbauer effect study of Fe_3Sn_2, J. Phys. F **8**, 323 (1978).

[13] S. Nakatsuji, N. Kiyohara, and T. Higo, Large anomalous Hall effect in a non-collinear antiferromagnet at room temperature, Nature (London) **527**, 212 (2015).

[14] L. Ye, M. Kang, J. Liu, F. Von Cube, C. R. Wicker, T. Suzuki, C. Jozwiak, A. Bostwick, E. Rotenberg, D. C. Bell, L. Fu, R. Comin, and J. G. Checkelsky, Massive Dirac fermions in a ferromagnetic kagome metal, Nature (London) **555**, 638 (2018).

[15] N. Kiyohara, T. Tomita, and S. Nakatsuji, Giant anomalous Hall effect in the chiral antiferromagnet Mn_3Ge, Phys. Rev. Appl. **5**, 064009 (2016).

[16] A. K. Nayak, J. E. Fischer, Y. Sun, B. Yan, J. Karel, A. C. Komarek, C. Shekhar, N. Kumar, W. Schnelle, J. Kübler *et al.*, Large anomalous Hall effect driven by a nonvanishing Berry curvature in the noncolinear antiferromagnet Mn_3Ge, Sci. Adv. **2**, e1501870 (2016).

[17] J. Yan, X. Luo, H. Y. Lv, Y. Sun, P. Tong, W. J. Lu, X. B. Zhu, W. H. Song, and Y. P. Sun, Room-temperature angular-dependent topological Hall effect in chiral antiferromagnetic Weyl semimetal Mn_3Sn, Appl. Phys. Lett. **115**, 102404 (2019).

[18] K. Kuroda, T. Tomita, M.-T. Suzuki, C. Bareille, A. Nugroho, P. Goswami, M. Ochi, M. Ikhlas, M. Nakayama, S. Akebi *et al.*, Evidence for magnetic Weyl fermions in a correlated metal, Nat. Mater. **16**, 1090 (2017).

[19] Z. Lin, J.-H. Choi, Q. Zhang, W. Qin, S. Yi, P. Wang, L. Li, Y. Wang, H. Zhang, Z. Sun, L. Wei, S. Zhang, T. Guo, Q. Lu, J.-H. Cho, C. Zeng, and Z. Zhang, Flat bands and emergent ferromagnetic ordering in Fe_3Sn_2 kagome lattices, Phys. Rev. Lett. **121**, 096401 (2018).

[20] J.-X. Yin, S. S. Zhang, G. Chang, Q. Wang, S. S. Tsirkin, Z. Guguchia, B. Lian, H. Zhou, K. Jiang, I. Belopolski *et al.*, Negative flat band magnetism in a spin–orbit-coupled correlated kagome magnet, Nat. Phys. **15**, 443 (2019).

[21] M. Kang, L. Ye, S. Fang, J.-S. You, A. Levitan, M. Han, J. I. Facio, C. Jozwiak, A. Bostwick, E. Rotenberg *et al.*, Dirac fermions and flat bands in the ideal kagome metal FeSn, Nat. Mater. **19**, 163 (2020).

[22] Z. Chen, M. Li, C. Liu, Z. Ma, Y. Han, J. Gao, W. Wei, Z. Sheng, and H. Du, Magnetic domain structure in ferromagnetic kagome metal $DyMn_6Sn_6$, Front. Phys. **9**, 685510 (2021).

[23] J. Zeng, M. Lu, H. Liu, H. Jiang, and X. Xie, Realistic flat-band model based on degenerate p-orbitals in two-dimensional ionic materials, Sci. Bull. **66**, 765 (2021).

[24] B. C. Sales, W. R. Meier, A. F. May, J. Xing, J.-Q. Yan, S. Gao, Y. H. Liu, M. B. Stone, A. D. Christianson, Q. Zhang, and M. A. McGuire, Tuning the flat bands of the kagome metal CoSn with Fe, In, or Ni doping, Phys. Rev. Mater. **5**, 044202 (2021).

[25] Z. Wang, Y.-X. Jiang, J.-X. Yin, Y. Li, G.-Y. Wang, H.-L. Huang, S. Shao, J. Liu, P. Zhu, N. Shumiya, M. S. Hossain, H. Liu, Y. Shi, J. Duan, X. Li, G. Chang, P. Dai, Z. Ye, G. Xu, Y. Wang *et al.*, Electronic nature of chiral charge order in the kagome superconductor CsV_3Sb_5, Phys. Rev. B **104**, 075148 (2021).

[26] F. H. Yu, T. Wu, Z. Y. Wang, B. Lei, W. Z. Zhuo, J. J. Ying, and X. H. Chen, Concurrence of anomalous Hall effect and charge density wave in a superconducting topological kagome metal, Phys. Rev. B **104**, L041103 (2021).

[27] Z. Zhang, Z. Chen, Y. Zhou, Y. Yuan, S. Wang, J. Wang, H. Yang, C. An, L. Zhang, X. Zhu, Y. Zhou, X. Chen, J. Zhou, and Z. Yang, Pressure-induced reemergence of superconductivity in the topological kagome metal CsV_3Sb_5, Phys. Rev. B **103**, 224513 (2021).

[28] M. Shi, F. Yu, Y. Yang, F. Meng, B. Lei, Y. Luo, Z. Sun, J. He, R. Wang, Z. Jiang *et al.*, A new class of bilayer kagome lattice compounds with Dirac nodal lines and pressure-induced superconductivity, Nat. Commun. **13**, 2773 (2022).

[29] L. Yu, C. Wang, Y. Zhang, M. Sander, S. Ni, Z. Lu, S. Ma, Z. Wang, Z. Zhao, H. Chen, K. Jiang, Y. Zhang, H. Yang, F. Zhou, X. Dong, S. L. Johnson, M. J. Graf, J. Hu, H.-J. Gao, and Z. Zhao, Evidence of a hidden flux phase in the topological kagome metal CsV_3Sb_5, arXiv:2107.10714 [cond-mat.supr-con].

[30] C. Mielke III, D. Das, J.-X. Yin, H. Liu, R. Gupta, Y.-X. Jiang, M. Medarde, X. Wu, H. C. Lei, J. Chang, P. Dai, Q. Si, H. Miao, R. Thomale, T. Neupert, Y. Shi, R. Khasanov, M. Z. Hasan,

H. Luetkens, and Z. Guguchia, Time-reversal symmetry-breaking charge order in a kagome superconductor, Nature **602**, 245 (2022).

[31] Y. Li, Q. Wang, L. DeBeer-Schmitt, Z. Guguchia, R. D. Desautels, J.-X. Yin, Q. Du, W. Ren, X. Zhao, Z. Zhang, I. A. Zaliznyak, C. Petrovic, W. Yin, M. Z. Hasan, H. Lei, and J. M. Tranquada, Magnetic-field control of topological electronic response near room temperature in correlated kagome magnets, Phys. Rev. Lett. **123**, 196604 (2019).

[32] L. Ye, S. Fang, M. G. Kang, J. Kaufmann, Y. Lee, J. Denlinger, C. Jozwiak, A. Bostwick, E. Rotenberg, E. Kaxiras, D. C. Bell, O. Janson, R. Comin, and J. G. Checkelsky, A flat band-induced correlated kagome metal, arXiv:2106.10824 [cond-mat.mtrl-sci].

[33] I. Lyalin, S. Cheng, and R. K. Kawakami, Spin–orbit torque in bilayers of kagome ferromagnet Fe_3Sn_2 and Pt, Nano Lett. **21**, 6975 (2021).

[34] T. Neupert, M. M. Denner, J.-X. Yin, R. Thomale, and M. Z. Hasan, Charge order and superconductivity in kagome materials, Nat. Phys. **18**, 137 (2022).

[35] Y. Yang, R. Wang, M.-Z. Shi, Z. Wang, Z. Xiang, and X.-H. Chen, Symmetry-protected Dirac nodal lines and large spin Hall effect in a V_6Sb_4 kagome bilayer, Phys. Rev. B **105**, 155102 (2022).

[36] Z. Liu, M. Li, Q. Wang, G. Wang, C. Wen, K. Jiang, X. Lu, S. Yan, Y. Huang, D. Shen *et al.*, Orbital-selective Dirac fermions and extremely flat bands in frustrated kagome-lattice metal CoSn, Nat. Commun. **11**, 4002 (2020).

[37] M. Kang, S. Fang, L. Ye, H. C. Po, J. Denlinger, C. Jozwiak, A. Bostwick, E. Rotenberg, E. Kaxiras, J. G. Checkelsky *et al.*, Topological flat bands in frustrated kagome lattice CoSn, Nat. Commun. **11**, 4004 (2020).

[38] M. Li, Q. Wang, G. Wang, Z. Yuan, W. Song, R. Lou, Z. Liu, Y. Huang, Z. Liu, H. Lei *et al.*, Dirac cone, flat band and saddle point in kagome magnet YMn_6Sn_6, Nat. Commun. **12**, 3129 (2021).

[39] J.-X. Yin, W. Ma, T. A. Cochran, X. Xu, S. S. Zhang, H.-J. Tien, N. Shumiya, G. Cheng, K. Jiang, B. Lian *et al.*, Quantum-limit Chern topological magnetism in $TbMn_6Sn_6$, Nature (London) **583**, 533 (2020).

[40] L. Gao, S. Shen, Q. Wang, W. Shi, Y. Zhao, C. Li, W. Cao, C. Pei, J.-Y. Ge, G. Li, J. Li, Y. Chen, S. Yan, and Y. Qi, Anomalous Hall effect in ferrimagnetic metal RMn_6Sn_6 (R = Tb, Dy, Ho) with clean Mn kagome lattice, Appl. Phys. Lett. **119**, 092405 (2021).

[41] F. Yu, D. Ma, W. Zhuo, S. Liu, X. Wen, B. Lei, J. Ying, and X. Chen, Unusual competition of superconductivity and charge-density-wave state in a compressed topological kagome metal, Nat. Commun. **12**, 3645 (2021).

[42] H. Li, T. T. Zhang, T. Yilmaz, Y. Y. Pai, C. E. Marvinney, A. Said, Q. W. Yin, C. S. Gong, Z. J. Tu, E. Vescovo, C. S. Nelson, R. G. Moore, S. Murakami, H. C. Lei, H. N. Lee, B. J. Lawrie, and H. Miao, Observation of unconventional charge density wave without acoustic phonon anomaly in kagome superconductors AV_3Sb_5 (A = Rb, Cs), Phys. Rev. X **11**, 031050 (2021).

[43] M. Tuniz, A. Consiglio, D. Puntel, C. Bigi, S. Enzner, G. Pokharel, P. Orgiani, W. Bronsch, F. Parmigiani, V. Polewczyk, P. D. C. King, J. W. Wells, I. Zeljkovic, P. Carrara, G. Rossi, J. Fujii, I. Vobornik, S. D. Wilson, R. Thomale, T. Wehling *et al.*, Dynamics and resilience of the charge density wave in a bilayer kagome metal, arXiv:2302.10699 [cond-mat.str-el].

[44] Q. Du, Z. Hu, M.-G. Han, F. Camino, Y. Zhu, and C. Petrovic, Topological Hall effect anisotropy in kagome bilayer metal Fe_3Sn_2, Phys. Rev. Lett. **129**, 236601 (2022).

[45] S. A. Ekahana, Y. Soh, A. Tamai, D. Gosálbez-Martínez, M. Yao, A. Hunter, W. Fan, Y. Wang, J. Li, A. Kleibert, C. A. F. Vaz, J. Ma, Y. Xiong, O. V. Yazyev, F. Baumberger, M. Shi, and G. Aeppli, Anomalous quasiparticles in the zone center electron pocket of the kagomé ferromagnet Fe_3Sn_2, arXiv:2206.13750 [cond-mat.str-el].

[46] W. Zhang, T. Citra Asmara, Y. Tseng, J. Li, Y. Xiong, V. N. Strocov, Y. Soh, T. Schmitt, and G. Aeppli, Spin waves in a ferromagnetic topological metal, arXiv:2302.01457 [cond-mat.str-el].

[47] Y.-F. Zhang, X.-S. Ni, T. Datta, M. Wang, D.-X. Yao, and K. Cao, Ab initio study of spin fluctuations in the itinerant kagome magnet FeSn, Phys. Rev. B **106**, 184422 (2022).

[48] D. Multer, J.-X. Yin, M. S. Hossain, X. Yang, B. C. Sales, H. Miao, W. R. Meier, Y.-X. Jiang, Y. Xie, P. Dai *et al.*, Imaging real-space flat band localization in kagome magnet FeSn, Communications Materials **4**, 17 (2023).

[49] H. Li, H. Zhao, Q. Yin, Q. Wang, Z. Ren, S. Sharma, H. Lei, Z. Wang, and I. Zeljkovic, Spin-polarized imaging of the antiferromagnetic structure and field-tunable bound states in kagome magnet FeSn, Sci. Rep. **12**, 14525 (2022).

[50] K. I. A. Khan, R. S. Yadav, H. Bangar, A. Kumar, N. Chowdhury, P. K. Muduli, and P. K. Muduli, Intrinsic anomalous Hall effect in thin films of topological kagome ferromagnet Fe_3Sn_2, Nanoscale **14**, 8484 (2022).

[51] S. Baidya, A. V. Mallik, S. Bhattacharjee, and T. Saha-Dasgupta, Interplay of magnetism and topological superconductivity in bilayer kagome metals, Phys. Rev. Lett. **125**, 026401 (2020).

[52] S. Cheng, I. Lyalin, A. J. Bishop, and R. K. Kawakami, Epitaxial growth and domain structure imaging of kagome magnet Fe_3Sn_2, arXiv:2105.12203 [cond-mat.mtrl-sci].

[53] A. Szasz, J. Motruk, M. P. Zaletel, and J. E. Moore, Chiral spin liquid phase of the triangular lattice Hubbard model: A density matrix renormalization group study, Phys. Rev. X **10**, 021042 (2020).

[54] E. Y. Andrei and A. H. MacDonald, Graphene bilayers with a twist, Nat. Mater. **19**, 1265 (2020).

[55] L. Yin, D. Zhang, C. Chen, G. Ye, F. Yu, B. R. Ortiz, S. Luo, W. Duan, H. Su, J. Ying, S. D. Wilson, X. Chen, H. Yuan, Y. Song, and X. Lu, Strain-sensitive superconductivity in the kagome metals KV_3Sb_5 and CsV_3Sb_5 probed by point-contact spectroscopy, Phys. Rev. B **104**, 174507 (2021).

[56] K. Fujiwara, Y. Kato, T. Seki, K. Nomura, K. Takanashi, Y. Motome, and A. Tsukazaki, Tuning scalar spin chirality in ultrathin films of the kagome-lattice ferromagnet Fe_3Sn, Commun. Mater. **2**, 113 (2021).

[57] Y. Li, C. Liu, G.-D. Zhao, T. Hu, and W. Ren, Two-dimensional multiferroics in a breathing kagome lattice, Phys. Rev. B **104**, L060405 (2021).

[58] A. Consiglio, T. Schwemmer, X. Wu, W. Hanke, T. Neupert, R. Thomale, G. Sangiovanni, and D. Di Sante, Van Hove tuning of AV_3Sb_5 kagome metals under pressure and strain, Phys. Rev. B **105**, 165146 (2022).

[59] Z. Zhang, J.-Y. You, X.-Y. Ma, B. Gu, and G. Su, Kagome quantum anomalous Hall effect with high Chern number and large band gap, Phys. Rev. B **103**, 014410 (2021).

[60] F. Crasto de Lima, R. H. Miwa, and E. Suárez Morell, Double flat bands in kagome twisted bilayers, Phys. Rev. B **100**, 155421 (2019).

[61] S. Fang, L. Ye, M. P. Ghimire, M. Kang, J. Liu, M. Han, L. Fu, M. Richter, J. van den Brink, E. Kaxiras, R. Comin, and J. G. Checkelsky, Ferromagnetic helical nodal line and Kane-Mele spin-orbit coupling in kagome metal Fe_3Sn_2, Phys. Rev. B **105**, 035107 (2022).

[62] E. Fradkin, *Field Theories of Condensed Matter Physics* (Cambridge University Press, Cambridge, England, 2013).

[63] M. Trescher and E. J. Bergholtz, Flat bands with higher Chern number in pyrochlore slabs, Phys. Rev. B **86**, 241111(R) (2012).

[64] N. Regnault and B. A. Bernevig, Fractional Chern insulator, Phys. Rev. X **1**, 021014 (2011).

[65] A. Lopez and E. Fradkin, Fractional quantum Hall effect and Chern-Simons gauge theories, Phys. Rev. B **44**, 5246 (1991).

[66] Y.-F. Wang, H. Yao, C.-D. Gong, and D. N. Sheng, Fractional quantum Hall effect in topological flat bands with Chern number two, Phys. Rev. B **86**, 201101(R) (2012).

[67] E. J. Bergholtz and Z. Liu, Topological flat band models and fractional Chern insulators, Int. J. Mod. Phys. B **27**, 1330017 (2013).

[68] A. M. Läuchli, Z. Liu, E. J. Bergholtz, and R. Moessner, Hierarchy of fractional Chern insulators and competing compressible states, Phys. Rev. Lett. **111**, 126802 (2013).

[69] S. Kourtis, T. Neupert, C. Chamon, and C. Mudry, Fractional Chern insulators with strong interactions that far exceed band gaps, Phys. Rev. Lett. **112**, 126806 (2014).

[70] Y.-L. Wu, N. Regnault, and B. A. Bernevig, Bloch model wave functions and pseudopotentials for all fractional Chern insulators, Phys. Rev. Lett. **110**, 106802 (2013).

[71] Y.-L. Wu, N. Regnault, and B. A. Bernevig, Haldane statistics for fractional Chern insulators with an arbitrary Chern number, Phys. Rev. B **89**, 155113 (2014).

[72] P. A. Lee, N. Nagaosa, and X.-G. Wen, Doping a Mott insulator: Physics of high-temperature superconductivity, Rev. Mod. Phys. **78**, 17 (2006).

[73] W. Zheng, J. Oitmaa, C. J. Hamer, and R. R. P. Singh, Order and disorder in the triangular-lattice $t-j-v$ model at $\frac{2}{3}$ electron density, Phys. Rev. B **70**, 020504(R) (2004).

[74] K. A. Chao, J. Spalek, and A. M. Oles, Kinetic exchange interaction in a narrow s-band, J. Phys. C **10**, L271 (1977).

[75] J. E. Hirsch, Attractive interaction and pairing in fermion systems with strong on-site repulsion, Phys. Rev. Lett. **54**, 1317 (1985).

[76] S. Gong, W. Zhu, and D. N. Sheng, Robust d-wave superconductivity in the square-lattice $t-j$ model, Phys. Rev. Lett. **127**, 097003 (2021).

[77] N. Dan Tung, A. A. Vladimirov, and N. M. Plakida, Electronic spectrum and superconductivity in the extended $t-j-V$ model, Physica C: Supercond. Appl. **587**, 1353900 (2021).

[78] I. Ichinose and T. Matsui, Mechanism of charge-spin separation in the $t-J$ model: Dynamics of $U(1)$ gauge theory with multiple gauge fields, Phys. Rev. B **51**, 11860 (1995).

[79] I. Ichinose, T. Matsui, and M. Onoda, Effective gauge-field theory of the $t-J$ model in the charge-spin separated state and its transport properties, Phys. Rev. B **64**, 104516 (2001).

[80] N. Read and D. M. Newns, A new functional integral formalism for the degenerate Anderson model, J. Phys. C **16**, L1055 (1983).

[81] M. B. Hastings, Lieb-Schultz-Mattis in higher dimensions, Phys. Rev. B **69**, 104431 (2004).

[82] A. V. Mallik, G. K. Gupta, V. B. Shenoy, and H. R. Krishnamurthy, Surprises in the $t-J$ model: Implications for cuprates, Phys. Rev. Lett. **124**, 147002 (2020).

[83] H. Luo, Q. Gao, H. Liu, Y. Gu, D. Wu, C. Yi, J. Jia, S. Wu, X. Luo, Y. Xu, L. Zhao, Q. Wang, H. Mao, G. Liu, Z. Zhu, Y. Shi, K. Jiang, J. Hu, Z. Xu, and X. J. Zhou, Electronic nature of charge density wave and electron-phonon coupling in kagome superconductor KV_3Sb_5, Nat. Commun. **13**, 273 (2022).

[84] P. Weinberg and M. Bukov, QuSpin: A Python package for dynamics and exact diagonalisation of quantum many body systems part I: Spin chains, SciPost Phys. **2**, 003 (2017).

[85] P. Weinberg and M. Bukov, QuSpin: A Python package for dynamics and exact diagonalisation of quantum many body systems. Part II: Bosons, fermions and higher spins, SciPost Phys. **7**, 020 (2019).

[86] http://symmetry.jacobs-university.de/.

[87] M. Sigrist, Introduction to unconventional superconductivity, AIP Conf. Proc. **789**, 165 (2005).

[88] A. Dalal, J. Ruhman, and V. Kozii, The field theory of a superconductor with repulsion, arXiv:2308.05150 [cond-mat.supr-con].